applied sciences

MDPI

Article

Strain-Controlled Electronic and Magnetic Properties of Janus Nitride MXene Monolayer $MnCrNO_2$

Wentao Yue [1,2], Jun Shan [1,2], Runxian Jiao [1,2], Lichuan Zhang [1,2], Yuanping Chen [1,2,*] and Dong Hao [1,2,3,*]

[1] School of Physics and Electronic Engineering, Jiangsu University, Zhenjiang 212013, China; 3210103053@stmail.ujs.edu.cn (W.Y.); 2212226005@stmail.ujs.edu.cn (J.S.); 2222126018@ujs.edu.cn (R.J.); lichuan.zhang@ujs.edu.cn (L.Z.)
[2] Jiangsu Engineering Research Center on Quantum Perception and Intelligent Detection of Agricultural Information, Zhenjiang 212013, China
[3] Changzhou EGING PV Technology Co., Ltd., Changzhou 213200, China
* Correspondence: chenyp@ujs.edu.cn (Y.C.); hao@ujs.edu.cn (D.H.)

Abstract: Two-dimensional (2D) van der Waals (vdW) magnetic materials show potential for the advancement of high-density, energy-efficient electronic and spintronic applications in future memory and computation. Here, by using first-principles density functional theory (DFT) calculations, we predict a new 2D Janus nitride MXene $MnCrNO_2$ monolayer. Our results suggest that the optimized $MnCrNO_2$ monolayer possesses a hexagonal structure and exhibits good dynamical stability. The intrinsic monolayer $MnCrNO_2$ exhibits semiconductive properties and adopts a ferromagnetic ground state with an out-of-plane easy axis. It can sustain strain effects within a wide range of strains from −10% to +8%, as indicated by the phonon dispersion spectra. Under the biaxial tensile strain, a remarkable decrease in the bandgap of the $MnCrNO_2$ is induced, which is attributed to the distinct roles played by Mn and Cr in the VBM or CBM bands. Furthermore, when the compressive strain reaches approximately −8%, the magnetic anisotropy undergoes a transition from an out-of-plane easy axis to an in-plane easy axis. This change is mainly influenced by the efficient hybridization of the d orbitals, particularly in Mn atoms. Our study of the Janus MXene $MnCrNO_2$ monolayer indicates its potential as a promising candidate for innovative electronic and spintronic devices; this potential is expected to create interest in its synthesis.

Keywords: MXenes; 2D materials; electronic properties; magnetic anisotropy; strain

Citation: Yue, W.; Shan, J.; Jiao, R.; Zhang, L.; Chen, Y.; Hao, D. Strain-Controlled Electronic and Magnetic Properties of Janus Nitride MXene Monolayer $MnCrNO_2$. *Appl. Sci.* **2024**, *14*, 8427. https://doi.org/10.3390/app14188427

Academic Editor: Zhibin Yang

Received: 28 July 2024
Revised: 7 September 2024
Accepted: 10 September 2024
Published: 19 September 2024

1. Introduction

Following the groundbreaking discovery of graphene, many two-dimensional (2D) materials have entered people's vision for their unique electronic and magnetic properties and promising applications in nanoscale devices. Various types of 2D materials, such as transition metal dichalcogenides (TMDs), silicene, and phosphorene, have been synthesized so far [1–3]. These materials exhibit a wide range of physical properties that are being actively sought to fabricate high-performance electronic devices. While efforts in this area have been focused on the investigation of 2D semiconductors and optoelectronic or thermoelectric materials [4,5], 2D magnetic materials remain largely unexplored. Theoretically, 2D magnetic materials are an ideal platform for investigating how the Hamiltonians of the fundamental magnetism models, such as the Ising, XY, and Heisenberg models, behave in the 2D limit [6]. In practice, robust and tunable magnetic properties in 2D materials can be valuable in quantum computation, logic and memory operations, spintronics, and other electronic devices where the spin degree of freedom of the carriers is manipulated [7–10]. The magnetic ground states of these materials can be controlled via proximity effects and moiré patterns, or by external perturbations, such as gating and strain [11–14]. For successful implementation in real devices, it is of the utmost importance to understand and exploit the control of the ground state via strain and gating [15]. In addition to tuning the carrier

spin degree of freedom in devices, the search for intrinsically magnetic 2D materials is also of fundamental interest in understanding the basic physics of spin processes.

One class comprising 2D materials that are simultaneously robust, adjustable, and intrinsically magnetic, namely MXenes, is considered to be of research value in spin electronic devices. With the general formula of $M_{n+1}X_nT_x$ (where M represents transition metal, X represents C/N, and T is O/OH/F, n = 1–4), MXenes have rich tunability, including compositional tunability, elemental flexibility, and 2D crystallinity, allowing the fine tuning of desirable magnetic properties [16–19]. In addition, some published works have suggested that MXenes' tunable electronic and magnetic properties can be tailored remarkably via surface functionalization. For example, K. Yusupov et al. pointed out that metallic Nb_2CO_2 can be transformed into a semiconductor by the substitution of carbon with nitrogen [20]. In some recent theoretical reports, the effects of different surface terminating species on work function and electronic, vibrational, and thermal properties have been explored; they commonly include O, OH, NH, N, S, F, Cl, Br, I, which are bonded to the outer layer M atoms [20,21]. The experimental work also demonstrates that phosphorous (P) doping on the surface has proved effective in improving the electrochemical properties [22]. These studies provide a guide for researchers who are exploring relevant properties of MXenes. However, there are few reports on double-M 2D nitride MXenes (M'M''Xene) so far. B. Anasori et al. and L. Wang et al. have envisioned in theory that the layering effect owing to different types of M atoms will be even more pronounced [23,24]. Such layering is expected to play a crucial role in improving the properties of many promising 2D magnetic materials and devices. A good example in this category is the implementation of out-of-plane mirror symmetry breaking, i.e., 2D Janus MXenes, which would be an interesting issue due to atomic configuration of M layers in MXenes. Over the past few years, it has been found that the unique characteristics of 2D Janus MoSSe, the 2D Janus TMDC that was first prepared, can lead to its novel phenomena, such as Rashba spin splitting [25–28], piezoelectric polarization [25,27,28], second-harmonic generation [25,29], catalytic effects [25,26,30], and long carrier recombination [26,29–31].

Thus, motivated by the points discussed above, we report the possible existence of a Janus nitride MXene monolayer $MnCrNO_2$. Our exploration includes the structural, electronic, and magnetic properties of Janus MXene $MnCrNO_2$ with a set of first-principles calculations. In addition, mechanical tensile and compressive strain is introduced to probe its effects on the electronic and magnetic properties of monolayer $MnCrNO_2$. A significant change in the bandgap occurs in the 2D ferromagnetic $MnCrNO_2$ when tensile strain is applied and increased up to +8%. A complex dependence of these physical properties on strain induces the distinct evolution of the magnetic anisotropy energies (MAE), which can be accounted for mainly by the contribution from efficient hybridization of the $d_{xy}/d_{x^2-y^2}$ and d_{yz}/d_{z^2} orbitals of both Cr and Mn atoms. The MAE can be modulated from negative to positive within the applied strain range of −10% to 10%. All these findings indicate that the stable Janus MXene $MnCrNO_2$ holds great potential for high-performance practical spintronic application under strain.

2. Methods

Our density functional theory (DFT) calculations are carried out using the Vienna ab initio Simulation Package (VASP) [32,33]. Projector-augmented wave (PAW) pseudopotentials [34] are used with a kinetic energy cutoff of 500 eV for plane wave expansions. The Perdew–Burke–Ernzerhof (PBE) generalized gradient approximation (GGA) [35] is used to approximate the exchange-correlation functional. As validations, the hybrid functional HSE06 is also employed. Dudarev's GGA+U approach is employed to address the strong correlation influence on Cr and Mn transition metal atoms, requiring all electronic structure calculations and geometry relaxations to be performed with the spin-polarized DFT+U correction [36–38]. A U value of 4 eV is used for Cr and Mn, as is typical in the literature [39,40], for the on-site Coulombic repulsion. The convergence criterion for structural relaxations of the unit cell is 10^{-6} eV for total energies and 0.001 eV·A^{-1} for the force on each atom. A

vacuum layer of 25 Å along the c-axis, perpendicular to the surface, is utilized to prevent spurious interactions between adjacent periodic slabs. The first Brillouin zone is sampled within a set of 12 × 12 × 1 and 15 × 15 × 1 Γ-centered Monkhorst–Pack scheme k-point meshes [41] for structural optimizations and electronic structure calculations, respectively. Spin–orbit coupling (SOC) is included during the electronic structure and MAE calculations. To check the phonon dispersion and the dynamic stability, we perform the density functional perturbation theory (DFPT), as embedded in the Phonopy package [42–45].

3. Results

3.1. Structural Properties and Stability

The calculated ground-state structural configuration of pristine MXene $MnCrNO_2$ with fully relaxed geometry is discovered to have hexagonal symmetry and to belong to the *P3m*1 space group (No. 156). The side and top views of the structure are shown in Figure 1a, in which the $MnCrNO_2$ monolayer takes a fivefold layered structure, i.e., O-Mn-N-Cr-O. The primitive cell contains one Mn, one Cr, one N, and two O atoms, where the Mn atoms, the Cr atoms, and the sandwiched N atoms form a trigonal lattice, as shown in the top view. Structurally, the $MnCrNO_2$ monolayer is thus similar to the Mn_2NO_2 or Cr_2NO_2 monolayer [6,46]. The optimized lattice parameter of the monolayer $MnCrNO_2$ is a = 2.97 Å. The other relevant parameters with regard to the bond angles and bond lengths are listed in Table 1.

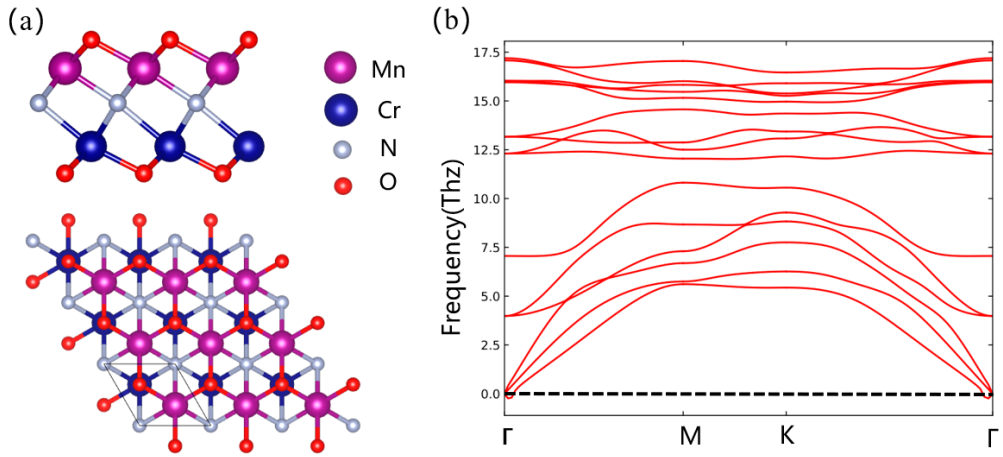

Figure 1. (**a**) Top and side view of the Janus monolayer $MnCrNO_2$. Purple, blue, grey, and red spheres represent Mn, Cr, N, and O atoms, respectively. (**b**) Phonon spectrum of the monolayer $MnCrNO_2$.

Table 1. The fully optimized bond angles and bond lengths for the Janus monolayer $MnCrNO_2$.

Bond	Length (Å)	Bond	Angle (°)
O-Cr	1.932	O-Cr-N	87.004
Cr-N	2.228	Cr-N-Mn	91.610
N-Mn	2.058	N-Mn-Mn	84.047
Mn-O	1.956		

To inspect its stability, we also calculate the phonon spectrum of the monolayer $MnCrNO_2$, as shown in Figure 1b. The phonon dispersion contains tiny imaginary frequencies resulting from common numerical simulation instabilities, but these imaginary frequencies only appear in a small region around the Γ point; they are related to long-wave fluctuations, occupying 0.4% of the total phonon density of states (DOS), and can be reasonably ignored. Such cases were also reported in other 2D materials [47,48]. Therefore, the $MnCrNO_2$ monolayer is thermally stable.

3.2. Magnetic and Electronic Properties

To determine the magnetic ground state of the $MnCrNO_2$ monolayer, we construct a monolayer supercell with 4-unit cells ($4 \times 1 \times 1$) and consider one ferromagnetic (FM) and all possible antiferromagnetic (AFM) configurations within this supercell. The initial on-site magnetic moments are set as 4 μ_B for each Mn and Cr atom and as nonmagnetic for each N and O atom. Figure 2 shows the FM configuration and the two AFM configurations at the magnetic ground states. Among these three magnetic configurations, the FM state takes the lowest energy and is thus the ground state, while the AFM1 and AFM2 configurations take the higher energy, i.e., 406.89 meV and 585.84 meV higher than that of the FM configuration. The monolayer $MnCrNO_2$ at the FM state exhibits a total magnetization of about 6.0 μ_B per primitive cell, with 3.4 μ_B attributed to the magnetization of the Mn atom and 3.0 μ_B from that of Cr, indicating their dominant roles in the magnetism of $MnCrNO_2$. Additionally, the N and O atoms contribute small negative magnetic moments (approximately -0.4 μ_B), primarily due to the spin polarization of their p orbitals caused by the p-d hybridization with neighboring magnetic Mn and Cr atoms, as evidenced by the spin-resolved projected density of states (PDOS) in Figure S1.

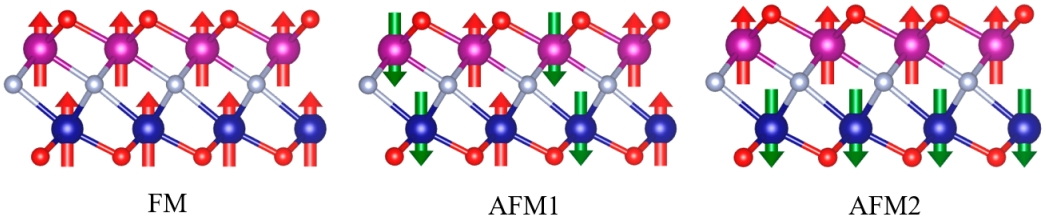

Figure 2. Side view of the three magnetic configurations. The red and green arrows represent spin-up and spin-down, respectively.

In order to further comprehend the relationship between the magnetic and electronic properties, the spin-polarized band structures and density of states are then calculated based on both PBE functional and hybrid-functional HSE06, as depicted in Figure 3. Near the Fermi level are the spin-majority bands, exhibiting a semiconducting characteristic, which is unlike that of the previously reported metallic MXenes, with an indirect bandgap of 0.69 (1.49) eV, as determined by the GGA-PBE (HSE06) functional. In other words, both the valence band maximum (VBM) and the conduction band minimum (CBM) are spin-up states despite their different locations. The spin-resolved PDOS in Figure S1a shows in more detail that the VBM bands are determined by the significant overlap between the Cr-3d and O-2p orbitals over a large energy range. In contrast, for the CBM bands, there is a similar 3d–2p overlap, but with a greater proportion accounted for by the Mn-3d orbitals. Overall, these electronic properties remain similar for Hubbard U = 1 eV, 2 eV, and 3 eV for Mn and Cr, except for the small and predictable changes in the bandgap, as shown in Figure S2. The different roles played by 3d transition metal atoms (Mn and Cr) in the VBM or CBM bands of monolayer $MnCrNO_2$ demonstrate the potential and effectiveness of energy band engineering for Janus $MnCrNO_2$ through stacking configurations, pressure, strain, and other methods.

3.3. Effect of Biaxial Strains

The effects of biaxial strain on the 2D supercell are modeled by stretching and compressing along the a-axis and b-axis. We investigate the impact of biaxial strains ranging from -10% to $+10\%$ on the magnetic and electronic properties of monolayer Janus $MnCrNO_2$. Here, the applied biaxial strain is defined as

$$\varepsilon = \frac{a - a_0}{a_0} \times 100\%,$$

where a and a_0 are the unstrained and strained lattice constants of the monolayer $MnCrNO_2$, respectively. The negative and positive values of ε correspond to the biaxial compressive and tensile strains, respectively.

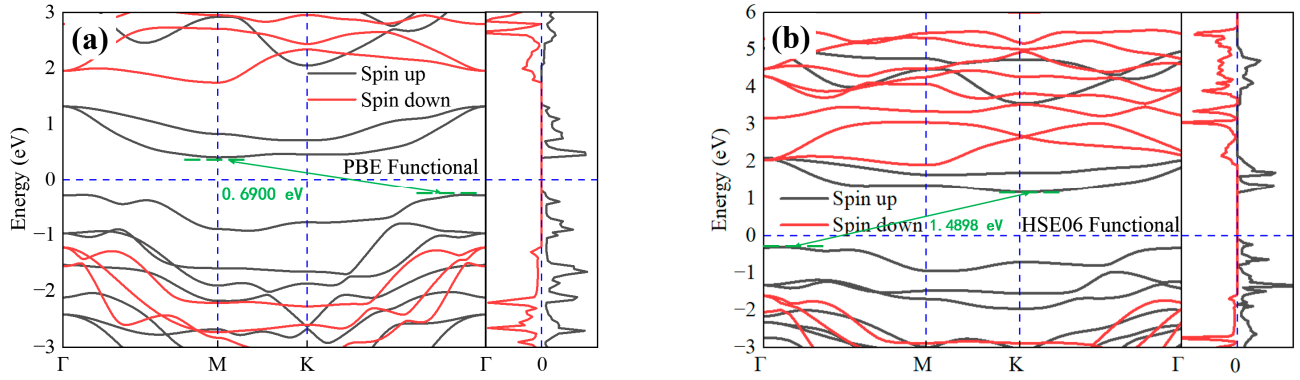

Figure 3. Spin-polarized band structures and DOS of the $MnCrNO_2$ monolayer using (**a**) PBE functional and (**b**) hybrid-functional HSE06, respectively. In panel (**a**), the CBM is situated at the M point, while the VBM is located close to the Γ point along the K–Γ path, indicated in green. In contrast, the CBM in (**b**) is located close to the K point, and the VBM is near the Γ point. The Fermi level is denoted by a horizontal dashed line at zero energy. The black and red lines represent spin-up and spin-down, respectively.

First, we check the biaxial strain (both tensile and compressive strains) effect on the thermodynamic stability of monolayer Janus $MnCrNO_2$. It can be seen in Figure S3 that the monolayer structure is thermodynamically stable for both the strain-free condition and the compression strains, without any imaginary frequency for all the wave vectors in the entire Brillouin zone. For the tensile strains from +2% to +8%, the tiny imaginary frequencies, which may correspond to the transverse acoustic (TA) modes, only appear in a narrow region near the Γ point. This kind of stability is generally similar to that of the strain-free sample. When increased to +10%, the compressive strain results in more significant negative frequency modes, as shown in Figure S3e, implying the possible structural instability.

We then study the effect of strain on the band structure of the $MnCrNO_2$ monolayer. The electronic band structures are calculated with applied strain ranging from −10% to +10%, at 2% intervals. Figure 4 illustrates the bandgaps and band structures of the strained $MnCrNO_2$ monolayer under different strains. As shown in Figure 4a, the application of various strains can effectively tune the bandgap of the $MnCrNO_2$ monolayer obtained with the PBE and HSE06 functionals. With strains ranging from −8% to +8%, the bandgap decreases significantly from 1.33 eV to 0.16 eV within the PBE framework. Although such a decrease may lead to a transition from semiconductor to metal when the tensile strain reaches +10%, the monolayer might be unstable due to imaginary frequencies in the phonon modes. This behavior is distinct from the electronic properties of the MXene counterpart, $WCrCO_2$ [49], but resembles those of TMDs when they are tuned by applying mechanical strains [50]. The subtle difference lies in the orbital contribution. For TMDs, the subsequent semiconductor-to-metal transition is achieved due to the transition between the d_{z^2} orbitals, while in the $MnCrNO_2$ monolayer, several 3d orbitals and O-2p orbitals work together to drive the transition, as can be verified in the Bader charge analysis in Table S1. The band structures under −10% biaxial strain and those under +8% biaxial strain are shown in Figure 4b–e, respectively. Within the framework of the HSE06 functional, the bandgap of the $MnCrNO_2$ monolayer reaches a maximum, i.e., 1.68 eV, under −4% compressive strain. For strains from −4% to +10%, the bandgaps calculated by the HSE06 functional are larger than those by the PBE functional. The PBE- and HSE06-based band structures under strains of ±2%, ±4%, ±6%, and −8% are presented in Figures S4 and S5, respectively. What differs from the PBE-based results is that the CBM obtained within HSE06 under compressive strains from −4% to −10% is spin-down, as shown in Figure S5b–d.

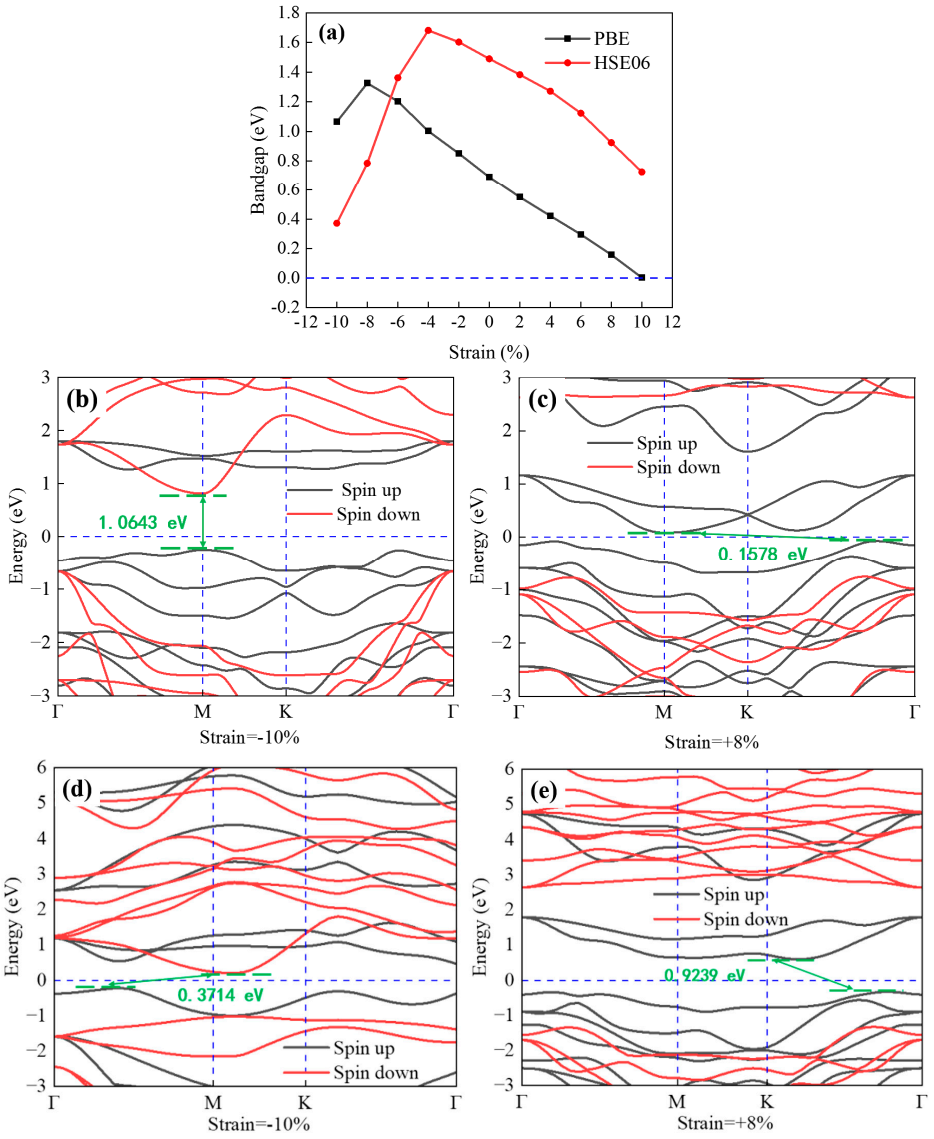

Figure 4. (**a**) Evolution of bandgaps of Janus monolayer $MnCrNO_2$ under various biaxial strains ranging from −10% to +10%. Black lines and red lines represent the results from the PBE and HSE06 functionals, respectively. The blue dashed line indicates the position of zero bandgap. (**b**,**c**) The PBE-based band structures of monolayer $MnCrNO_2$, corresponding to −10% compressive strain and +8% tensile strain, respectively. Both the CBM and the VBM in (**b**) are located at the M point, forming a direct gap. (**d**,**e**) The HSE06-based band structures of $MnCrNO_2$, corresponding to −10% compressive strain and +8% tensile strain, respectively. The Fermi level is denoted by a horizontal dashed line at zero energy.

The analysis above reveals that both the compressive and tensile mechanical strains significantly impact the band structures and interfacial charge transfer. In the following section, we further explore how strain influences the magnetic anisotropy. MAE, defined as the difference between energies corresponding to the magnetization in the in-plane (ab-plane) and out-of-plane direction (c-direction), is calculated using the following equation:

$$\mathrm{MAE} = E_{\mathrm{in}} - E_{\mathrm{out}},$$

where E_{in} and E_{out} represent the total energy of the in-plane and out-of-plane magnetic moment configurations of monolayer Janus $MnCrNO_2$, respectively. Therefore, a positive (negative) MAE value indicates that the ferromagnets have an out-of-plane (in-plane) spin

polarization direction. Since the FM magnetic configuration takes the ground state among the three magnetic configurations, here we focus on the MAE of the FM configuration for simplicity. Figure 5a demonstrates the variation in MAE under applied biaxial strains. The minimum MAE of −58 μeV is observed under a compressive strain of −10% and then gradually increases to 269 μeV under a tensile strain of 10%. An interesting observation is that the MAE becomes negative at around and below −8% compressive strain, indicating a switch of the magnetic easy axis from the out-of-plane to the in-plane direction. Thus, the applied strains can regulate both the electronic properties and the magnetization of the monolayer $MnCrNO_2$ simultaneously.

Figure 5b presents the increase in magnetic moment of both the Mn and Cr atoms in monolayer $MnCrNO_2$ with the FM state under applied biaxial strain. The magnetic moment of Mn ranges from 3.15 μ_B at −10% compressive strain to 3.90 μ_B at +10% tensile strain, whereas the range of magnetic moment for Cr is only one-fifth, i.e., from 2.99 μ_B to 3.14 μ_B. The probable reason, as can be inferred from Table S1, is that the Cr-3d and O-2p orbitals have more overlap than the Mn-3d and O-2p. The Mn-3d orbitals are mainly more localized near the Fermi level and are thus more influenced by applied strain, resulting in a larger variation in magnetic moment. The magnetic moment of Mn and Cr in the case of the AFM1 and AFM2 configurations is also evaluated and shown in Figure 5c,d, respectively, given that these two configurations can be meta-stable. These variations are almost the same as the results with the FM state. The slight difference lies in the magnetic moment of Cr atoms within the AFM2 configuration, whose values are higher overall than those with the FM and AFM2 state, as shown in Figure 5d.

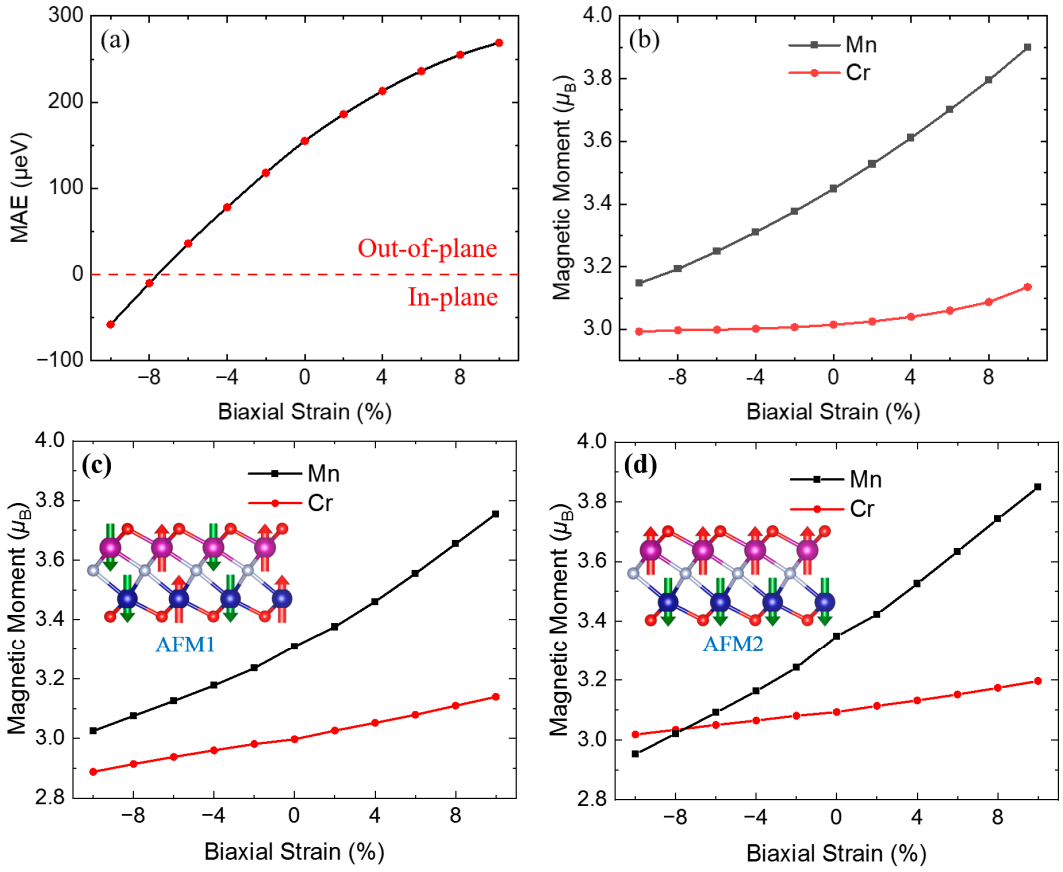

Figure 5. (**a**) Evolution of MAE of Janus monolayer $MnCrNO_2$ under biaxial strains ranging from −10% to +10%. A switch of the magnetic easy axis occurs at around −8% compressive strain, transitioning from an out-of-plane to an in-plane direction. (**b**–**d**) Variations in magnetic moment per Mn or Cr atom under biaxial strain, in units of μ_B. Insets of (**c**,**d**) are the schematics of the AFM1 and AFM2 magnetic configurations.

Since the 3d orbitals of transition metal atoms around the Fermi level mainly determine the magnetic moments in the Janus monolayer $MnCrNO_2$ and are relevant to the direction of MAE accordingly, we now discuss the 3d-orbital-resolved MAE of Mn and Cr atoms in the $MnCrNO_2$ monolayer under biaxial strains. Based upon the second order perturbation theory, MAE has the following expression [51,52]:

$$\mathrm{MAE} = \xi^2 \left[\sum_{u,o} \frac{\langle u|L_x|o\rangle^2}{E_u - E_o} - \frac{\langle u|L_z|o\rangle^2}{E_u - E_o} \right],$$

where ξ and u/o denote the strength of SOC and the energy eigenstates, and E_u (E_o) is the eigenvalues of the unoccupied (occupied) states. Therefore, MAE originates from the L_x/L_z operators and the hybridization between occupied and unoccupied states, as reported in [53]. Figure 6 shows the results of the 3d-orbital-resolved MAE of Mn and Cr atoms under both the strain-free condition and the −10% compressive strain, respectively. Obviously, the contribution of MAE mainly comes from the efficient hybridization of the $d_{xy}/d_{x^2-y^2}$ and d_{yz}/d_{z^2} orbitals of both Cr and Mn atoms. It can be seen that each $d_{xy}/d_{x^2-y^2}$ hybridized orbital leads to a negative difference of matrix elements, and conversely, the d_{xy}/d_{z^2} hybridization brings a positive value. As a result, the nature of magnetization, whether in-plane or out-of-plane, primarily depends on the competition between these two dominant hybridization effects. In addition, the matrix element difference between the other 3d orbitals, such as the d_{xz}/d_{yz} orbitals of Cr, d_{xy}/d_{xz}, and the $d_{yz}/d_{x^2-y^2}$ orbitals of Mn, also contributes slightly to the out-of-plane magnetic anisotropy with a positive sign.

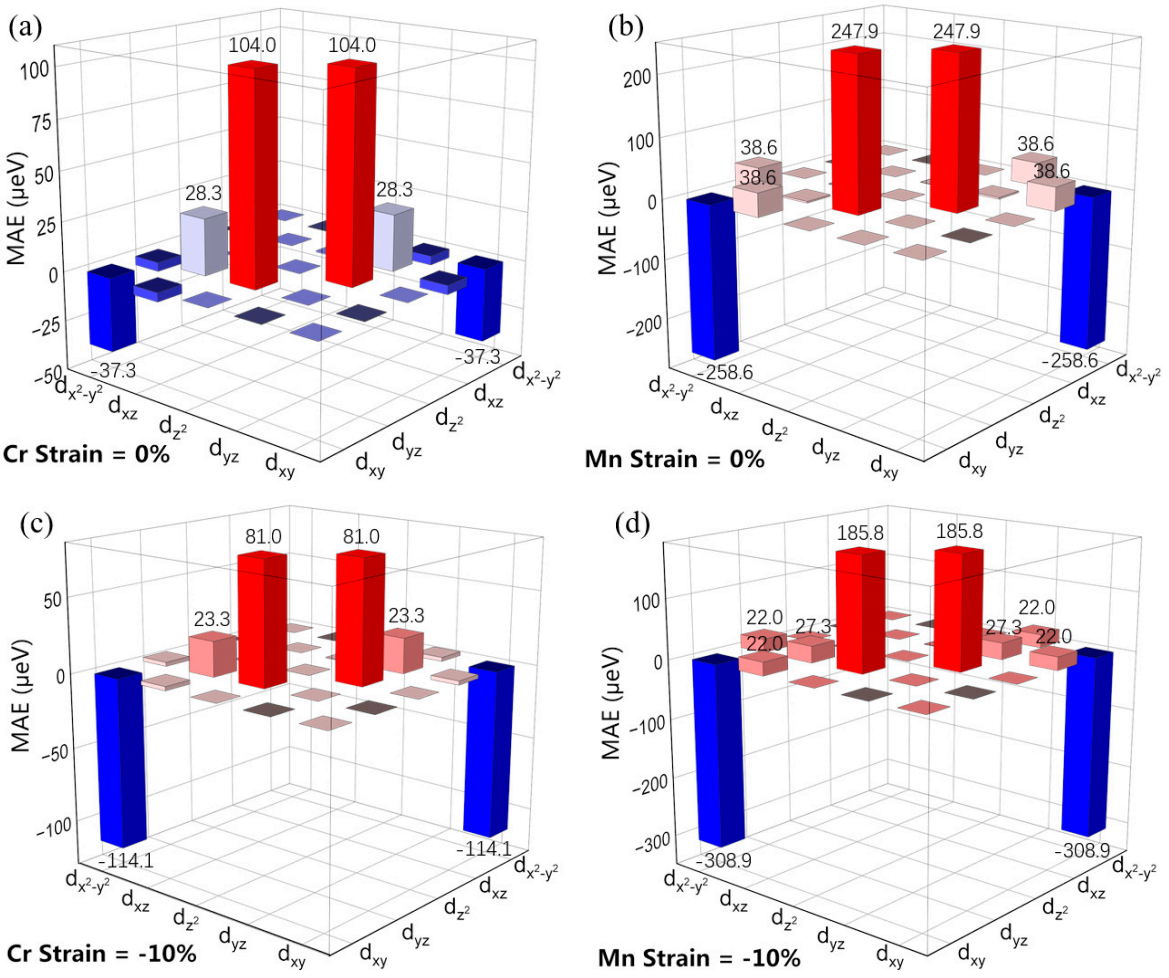

Figure 6. The 3d-orbital-resolved MAE of Cr and Mn atoms in the monolayer $MnCrNO_2$ under both strain-free condition (**a**,**b**) and −10% compressive strain (**c**,**d**), respectively.

Under the strain-free condition, as shown in Figure 6a,b, the out-of-plane magnetic anisotropy is governed by the d_{yz}/d_{z^2} hybridized orbitals, especially for Cr atoms, resulting in the out-of-plane magnetization of monolayer $MnCrNO_2$. On the other hand, under −10% compressive strain, Figure 6c,d shows that the in-plane $d_{xy}/d_{x^2-y^2}$ hybridization, particularly for Mn, enhances and dominates the in-plane magnetization of monolayer $MnCrNO_2$. The negative matrix element difference of the Mn $d_{xy}/d_{x^2-y^2}$ orbitals reaches −308.9 μeV. We also plotted the 3d-orbital-resolved MAE of Cr and Mn atoms under strains of −2%, −4%, −6%, and −8%, respectively, as shown in Figure S6. All these MAE values undergo a uniform change, and the sum of the negative MAE is superior to that of the positive MAE when the compressive strain is down to −8%. The switch of the magnetic easy axis in the Janus monolayer $MnCrNO_2$ is attributed to the hybridized 3d orbitals of Mn and Cr, as the contribution from the p orbitals of the N and O atoms to MAE is relatively weak compared with the 3d orbitals, despite the slight magnetic moments in N and O. This can be confirmed by the p-orbital-resolved MAE of the N and O atoms in Figure S7.

4. Conclusions

In summary, the structural, electronic, and magnetic properties of the Janus MXene $MnCrNO_2$ monolayer under various biaxial strains were proposed and investigated in detail using density functional theory calculations. It was found that the optimized $MnCrNO_2$ monolayer possesses a hexagonal structure with a *P*3*m*1 space group and exhibits good dynamical stability. The intrinsic Janus monolayer $MnCrNO_2$ is semiconductive and adopts the ferromagnetic ground state with an out-of-plane easy axis. The phonon dispersion spectra show that this monolayer structure can sustain strain effects within a wide range of strains from −10% to +8%. By applying biaxial tensile strain, we can induce a decline in the bandgap in the 2D semiconductive $MnCrNO_2$, attributed to the distinct roles played by Mn and Cr in the VBM or CBM bands. Furthermore, the magnetic anisotropy undergoes a transition from an out-of-plane easy axis to an in-plane easy axis when the applied compressive strain reaches nearly −8%. This in-plane magnetization is primarily influenced by the efficient hybridization of the d orbitals, particularly in Mn atoms. We anticipate that the prediction of the Janus $MnCrNO_2$ monolayer will offer a new avenue for exploring 2D magnetic materials with out-of-plane symmetry breaking and for future electronic and spintronic devices.

Supplementary Materials: The following supporting information can be downloaded at: https://www.mdpi.com/article/10.3390/app14188427/s1, Figure S1: Spin-resolved total density of states and projected density-of-states of each element of monolayer $MnCrNO_2$ when stain is applied at −10%, 0 and 10%; Figure S2: Spin-resolved projected density-of-states of each element of monolayer $MnCrNO_2$ for different U values for Mn and Cr; Figure S3: Phonon spectrum of the monolayer $MnCrNO_2$ under strain; Figure S4: Band structures of Janus monolayer $MnCrNO_2$ based upon PBE under strain; Figure S5: Band structures of Janus monolayer $MnCrNO_2$ based upon HSE06 under strain; Figure S6: The 3d-orbital-resolved MAE of Cr and Mn atoms in the Janus monolayer $MnCrNO_2$ under strains; Figure S7: The p-orbital-resolved MAE of N, O1 and O2 atoms in the monolayer $MnCrNO_2$; Table S1: The Bader charge transfer of X atom (X = Cr, Mn, N, O1, O2) under different strains from −10% to +10%, at 2% intervals.

Author Contributions: W.Y.: funding acquisition, conceptualization, data curation, investigation, writing—original draft; J.S.: investigation; R.J.: investigation; L.Z.: conceptualization, supervision; Y.C.: funding acquisition, resources, supervision; D.H.: conceptualization, investigation, writing—review and editing, supervision. All authors have read and agreed to the published version of the manuscript.

Funding: This research was supported by the National Natural Science Foundation of China (Grant No. 12174157 and 12347156), the Natural Science Foundation of Jiangsu Province (No. BK20230516), the Scientific Research Project of Jiangsu University (Grant No. 4111190003), the College Students' Innovation Training Program of Jiangsu Province of China (Grant No. 202310299023Z), and the College Students' Research Topics of Jiangsu Province of China (Grant No. Y21A075).

Institutional Review Board Statement: Not applicable.

Informed Consent Statement: Not applicable.

Data Availability Statement: The raw data supporting the conclusions of this article will be made available by the authors on request.

Conflicts of Interest: Author Dong Hao was employed by the company Changzhou EGING PV Technology Co., Ltd. The remaining authors declare that the research was conducted in the absence of any commercial or financial relationships that could be construed as a potential conflict of interest.

References

1. Butler, S.Z.; Hollen, S.M.; Cao, L.; Cui, Y.; Gupta, J.A.; Gutiérrez, H.R.; Heinz, T.F.; Hong, S.S.; Huang, J.; Ismach, A.F.; et al. Progress, Challenges, and Opportunities in Two-Dimensional Materials Beyond Graphene. *ACS Nano* **2013**, *7*, 2898–2926. [CrossRef] [PubMed]
2. Khazaei, M.; Arai, M.; Sasaki, T.; Chung, C.-Y.; Venkataramanan, N.S.; Estili, M.; Sakka, Y.; Kawazoe, Y. Novel Electronic and Magnetic Properties of Two-Dimensional Transition Metal Carbides and Nitrides. *Adv. Funct. Mater.* **2013**, *23*, 2185–2192. [CrossRef]
3. Wang, H.; Yuan, H.; Hong, S.S.; Li, Y.; Cui, Y. Physical and chemical tuning of two-dimensional transition metal dichalcogenides. *Chem. Soc. Rev.* **2015**, *44*, 2664–2680. [CrossRef]
4. Khandy, S.A. Inspecting the electronic structure and thermoelectric power factor of novel p-type half-Heuslers. *Sci. Rep.* **2021**, *11*, 20756. [CrossRef]
5. Wani, A.F.; Khandy, S.A.; Patra, L.; Srinivasan, M.; Singh, J.; Ali, A.M.; Islam, I.; Dhiman, S.; Kaur, K. Intrinsic and strain dependent ultralow thermal conductivity in novel AuX (X = Cu, Ag) monolayers for outstanding thermoelectric applications. *Phys. Chem. Chem. Phys.* **2023**, *25*, 21736–21747. [CrossRef]
6. Frey, N.C.; Kumar, H.; Anasori, B.; Gogotsi, Y.; Shenoy, V.B. Tuning Noncollinear Spin Structure and Anisotropy in Ferromagnetic Nitride MXenes. *ACS Nano* **2018**, *12*, 6319–6325. [CrossRef]
7. Wolf, S.A.; Awschalom, D.D.; Buhrman, R.A.; Daughton, J.M.; von Molnár, S.; Roukes, M.L.; Chtchelkanova, A.Y.; Treger, D.M. Spintronics: A Spin-Based Electronics Vision for the Future. *Science* **2001**, *294*, 1488–1495. [CrossRef] [PubMed]
8. Chang, C.-Z.; Zhang, J.; Feng, X.; Shen, J.; Zhang, Z.; Guo, M.; Li, K.; Ou, Y.; Wei, P.; Wang, L.-L.; et al. Experimental Observation of the Quantum Anomalous Hall Effect in a Magnetic Topological Insulator. *Science* **2013**, *340*, 167–170. [CrossRef]
9. Adachi, H. Ultrafast Spintronics: Back to basics. *Nat. Phys.* **2015**, *11*, 707–708. [CrossRef]
10. Sakai, S.; Majumdar, S.; Popov, Z.I.; Avramov, P.V.; Entani, S.; Hasegawa, Y.; Yamada, Y.; Huhtinen, H.; Naramoto, H.; Sorokin, P.B.; et al. Proximity-Induced Spin Polarization of Graphene in Contact with Half-Metallic Manganite. *ACS Nano* **2016**, *10*, 7532–7541. [CrossRef]
11. Deng, Y.; Yu, Y.; Song, Y.; Zhang, J.; Wang, N.Z.; Sun, Z.; Yi, Y.; Wu, Y.Z.; Wu, S.; Zhu, J.; et al. Gate-tunable room-temperature ferromagnetism in two-dimensional Fe_3GeTe_2. *Nature* **2018**, *563*, 94–99. [CrossRef] [PubMed]
12. Jiang, S.; Shan, J.; Mak, K.F. Electric-field switching of two-dimensional van der Waals magnets. *Nat. Mater.* **2018**, *17*, 406–410. [CrossRef] [PubMed]
13. Sun, W.; Wang, W.; Li, H.; Li, X.; Yu, Z.; Bai, Y.; Zhang, G.; Cheng, Z. $LaBr_2$ bilayer multiferroic moiré superlattice with robust magnetoelectric coupling and magnetic bimerons. *NPJ Comput. Mater.* **2022**, *8*, 159. [CrossRef]
14. Vijay, K.; Vavilapalli, D.S.; Arya, A.; Srivastava, S.K.; Singh, R.; Sagdeo, A.; Jha, S.N.; Kumar, K.; Banik, S. Magneto-strain effects in 2D ferromagnetic van der Waal material $CrGeTe_3$. *Sci. Rep.* **2023**, *13*, 8579. [CrossRef]
15. Burch, K.S.; Mandrus, D.; Park, J.-G. Magnetism in two-dimensional van der Waals materials. *Nature* **2018**, *563*, 47–52. [CrossRef]
16. Naguib, M.; Kurtoglu, M.; Presser, V.; Lu, J.; Niu, J.; Heon, M.; Hultman, L.; Gogotsi, Y.; Barsoum, M.W. Two-Dimensional Nanocrystals Produced by Exfoliation of Ti_3AlC_2. *Adv. Mater.* **2011**, *23*, 4248–4253. [CrossRef]
17. Anasori, B.; Lukatskaya, M.R.; Gogotsi, Y. 2D metal carbides and nitrides (MXenes) for energy storage. *Nat. Rev. Mater.* **2017**, *2*, 16098. [CrossRef]
18. Khazaei, M.; Ranjbar, A.; Arai, M.; Sasaki, T.; Yunoki, S. Electronic properties and applications of MXenes: A theoretical review. *J. Mater. Chem. C* **2017**, *5*, 2488–2503. [CrossRef]
19. Wong, Z.M.; Deng, T.; Shi, W.; Wu, G.; Tan, T.L.; Yang, S.-W. High performance photocatalytic and thermoelectric two-dimensional asymmetrically ordered Janus-like MXene alloys. *Mater. Adv.* **2020**, *1*, 1176–1185. [CrossRef]
20. Yusupov, K.; Björk, J.; Rosen, J. A systematic study of work function and electronic properties of MXenes from first principles. *Nanoscale Adv.* **2023**, *5*, 3976–3984. [CrossRef]
21. Björk, J.; Rosen, J. Functionalizing MXenes by Tailoring Surface Terminations in Different Chemical Environments. *Chem. Mater.* **2021**, *33*, 9108–9118. [CrossRef]
22. Minakshi, M.; Samayamanthry, A.; Whale, J.; Aughterson, R.; Shinde, P.A.; Ariga, K.; Shrestha, L.K. Phosphorous—Containing Activated Carbon Derived from Natural Honeydew Peel Powers Aqueous Supercapacitors. *Chem.—Asian J.* **2024**, e202400622. [CrossRef] [PubMed]

23. Anasori, B.; Xie, Y.; Beidaghi, M.; Lu, J.; Hosler, B.C.; Hultman, L.; Kent, P.R.C.; Gogotsi, Y.; Barsoum, M.W. Two-Dimensional, Ordered, Double Transition Metals Carbides (MXenes). *ACS Nano* **2015**, *9*, 9507–9516. [CrossRef] [PubMed]
24. Wang, L.; Hu, P.; Long, Y.; Liu, Z.; He, X. Recent advances in ternary two-dimensional materials: Synthesis, properties and applications. *J. Mater. Chem. A* **2017**, *5*, 22855–22876. [CrossRef]
25. Li, R.; Cheng, Y.; Huang, W. Recent Progress of Janus 2D Transition Metal Chalcogenides: From Theory to Experiments. *Small* **2018**, *14*, 1802091. [CrossRef]
26. Wei, Y.; Tang, X.; Shang, J.; Ju, L.; Kou, L. Two-dimensional functional materials: From properties to potential applications. *Int. J. Smart Nano Mater.* **2020**, *11*, 247–264. [CrossRef]
27. Yagmurcukardes, M.; Qin, Y.; Ozen, S.; Sayyad, M.; Peeters, F.M.; Tongay, S.; Sahin, H. Quantum properties and applications of 2D Janus crystals and their superlattices. *Appl. Phys. Rev.* **2020**, *7*, 011311. [CrossRef]
28. Zhang, L.; Yang, Z.; Gong, T.; Pan, R.; Wang, H.; Guo, Z.; Zhang, H.; Fu, X. Recent advances in emerging Janus two-dimensional materials: From fundamental physics to device applications. *J. Mater. Chem. A* **2020**, *8*, 8813–8830. [CrossRef]
29. Zheng, T.; Lin, Y.-C.; Yu, Y.; Valencia-Acuna, P.; Puretzky, A.A.; Torsi, R.; Liu, C.; Ivanov, I.N.; Duscher, G.; Geohegan, D.B.; et al. Excitonic Dynamics in Janus MoSSe and WSSe Monolayers. *Nano Lett.* **2021**, *21*, 931–937. [CrossRef]
30. Wang, J.; Shu, H.; Zhao, T.; Liang, P.; Wang, N.; Cao, D.; Chen, X. Intriguing electronic and optical properties of two-dimensional Janus transition metal dichalcogenides. *Phys. Chem. Chem. Phys.* **2018**, *20*, 18571–18578. [CrossRef]
31. Li, H.; Qin, Y.; Ko, B.; Trivedi, D.B.; Hajra, D.; Sayyad, M.Y.; Liu, L.; Shim, S.-H.; Zhuang, H.; Tongay, S. Anomalous Behavior of 2D Janus Excitonic Layers under Extreme Pressures. *Adv. Mater.* **2020**, *32*, 2002401. [CrossRef] [PubMed]
32. Kresse, G.; Furthmüller, J. Efficiency of ab-initio total energy calculations for metals and semiconductors using a plane-wave basis set. *Comp. Mater. Sci.* **1996**, *6*, 15–50. [CrossRef]
33. Kresse, G.; Furthmüller, J. Efficient iterative schemes for ab initio total-energy calculations using a plane-wave basis set. *Phys. Rev. B* **1996**, *54*, 11169–11186. [CrossRef]
34. Kresse, G.; Joubert, D. From ultrasoft pseudopotentials to the projector augmented-wave method. *Phys. Rev. B* **1999**, *59*, 1758–1775. [CrossRef]
35. Perdew, J.P.; Burke, K.; Ernzerhof, M. Generalized Gradient Approximation Made Simple. *Phys. Rev. Lett.* **1996**, *77*, 3865–3868. [CrossRef]
36. Dudarev, S.L.; Botton, G.A.; Savrasov, S.Y.; Humphreys, C.J.; Sutton, A.P. Electron-energy-loss spectra and the structural stability of nickel oxide: An LSDA+U study. *Phys. Rev. B* **1998**, *57*, 1505–1509. [CrossRef]
37. Zhou, F.; Cococcioni, M.; Marianetti, C.A.; Morgan, D.; Ceder, G. First-principles prediction of redox potentials in transition-metal compounds with LDA + *U*. *Phys. Rev. B* **2004**, *70*, 235121. [CrossRef]
38. Jain, A.; Hautier, G.; Ong, S.P.; Moore, C.J.; Fischer, C.C.; Persson, K.A.; Ceder, G. Formation enthalpies by mixing GGA and GGA+*U* calculations. *Phys. Rev. B* **2011**, *84*, 045115. [CrossRef]
39. Wu, Z.; Shen, Z.; Xue, Y.; Song, C. Strain-induced topological phase transition and enhanced Curie temperature in $MnBi_2Te_4/CrI_3$ heterojunction. *Phys. Rev. Mater.* **2022**, *6*, 014011. [CrossRef]
40. Wang, B.; Wu, Y.; Bai, Y.; Shi, P.; Zhang, G.; Zhang, Y.; Liu, C. Origin and regulation of triaxial magnetic anisotropy in the ferromagnetic semiconductor CrSBr monolayer. *Nanoscale* **2023**, *15*, 13402–13410. [CrossRef]
41. Monkhorst, H.J.; Pack, J.D. Special points for Brillouin-zone integrations. *Phys. Rev. B* **1976**, *13*, 5188–5192. [CrossRef]
42. Gonze, X.; Lee, C. Dynamical matrices, Born effective charges, dielectric permittivity tensors, and interatomic force constants from density-functional perturbation theory. *Phys. Rev. B* **1997**, *55*, 10355–10368. [CrossRef]
43. Oba, F.; Togo, A.; Tanaka, I.; Paier, J.; Kresse, G. Defect energetics in ZnO: A hybrid Hartree-Fock density functional study. *Phys. Rev. B* **2008**, *77*, 245202. [CrossRef]
44. Togo, A. First-principles Phonon Calculations with Phonopy and Phono3py. *J. Phys. Soc. Jpn.* **2022**, *92*, 012001. [CrossRef]
45. Togo, A.; Chaput, L.; Tadano, T.; Tanaka, I. Implementation strategies in phonopy and phono3py. *J. Phys. Condens. Matter* **2023**, *35*, 353001. [CrossRef] [PubMed]
46. Kumar, H.; Frey, N.C.; Dong, L.; Anasori, B.; Gogotsi, Y.; Shenoy, V.B. Tunable Magnetism and Transport Properties in Nitride MXenes. *ACS Nano* **2017**, *11*, 7648–7655. [CrossRef] [PubMed]
47. Qi, R.; Shi, R.; Li, Y.; Sun, Y.; Wu, M.; Li, N.; Du, J.; Liu, K.; Chen, C.; Chen, J.; et al. Measuring phonon dispersion at an interface. *Nature* **2021**, *599*, 399–403. [CrossRef]
48. Hao, D.; Wang, Y.; Tang, X.; Zhao, X.; An, Y.; Wang, W.; Li, J.; Shan, X.; Lu, X. Geometrical and magnetic properties of small titanium and chromium clusters on monolayer hexagonal boron nitride. *Phys. Chem. Chem. Phys.* **2023**, *25*, 6079–6088. [CrossRef]
49. Bafekry, A.; Akgenc, B.; Ghergherehchi, M.; Peeters, F.M. Strain and electric field tuning of semi-metallic character $WCrCO_2$ MXenes with dual narrow band gap. *J. Phys. Condens. Matter* **2020**, *32*, 355504. [CrossRef]
50. Johari, P.; Shenoy, V.B. Tuning the Electronic Properties of Semiconducting Transition Metal Dichalcogenides by Applying Mechanical Strains. *ACS Nano* **2012**, *6*, 5449–5456. [CrossRef]
51. Wang, D.-S.; Wu, R.; Freeman, A.J. First-principles theory of surface magnetocrystalline anisotropy and the diatomic-pair model. *Phys. Rev. B* **1993**, *47*, 14932–14947. [CrossRef] [PubMed]

52. Song, Y.; Wang, X.; Mi, W. Role of electron filling in the magnetic anisotropy of monolayer WSe_2 doped with 5*d* transition metals. *Phys. Rev. Mater.* **2017**, *1*, 074408. [CrossRef]
53. Wang, L.; Lin, Z.; An, Y. Tunable valley polarization, magnetic anisotropy and dipole moment for layered Janus 2H–VSSe with intrinsic room temperature ferromagnetism. *J. Alloys Compd.* **2021**, *854*, 157141. [CrossRef]